



# A multi-method investigation of the permeability structure of brittle fault zones with ductile precursors in crystalline rock

Julian Osten<sup>1</sup> · Tom Schaber<sup>1</sup> · Garri Gaus<sup>2</sup> · Pooya Hamdi<sup>1</sup> · Florian Amann<sup>1,3</sup> · Peter Achtziger-Zupančič<sup>1,3</sup>

Received: 4 August 2023 / Revised: 31 October 2023 / Accepted: 5 November 2023 / Published online: 25 January 2024  
© The Author(s) 2024, corrected publication 2024

## Abstract

Brittle faults and fault zones are among the most hydraulically active elements in predominantly impermeable crystalline host rock. They pose a significant challenge to underground infrastructure like nuclear waste repositories. Brittle fault zones frequently occur along pre-existing ductile shear zones as they introduce weakness planes in the rock. Four brittle fault zones of ductile origin were analyzed in the Rotondo Granite at the “BedrettoLab” in the Swiss Central Alps. Scanline mapping, rock sampling and permeability measurements using three different methods provide detailed insights into the heterogeneous fault zone architecture and hydrogeology. Average intact rock permeability is in the range of  $10^{-19}$  to  $10^{-17}$  m<sup>2</sup>. Fluid flow is channeled into single open or partially mineralized fractures of, at point-scale, up to  $10^{-14}$  m<sup>2</sup>, demonstrated by selective gas probe permeameter measurements and borehole hydraulic testing. Reduced permeabilities have been measured in close proximity to these permeable features, indicating alteration of and around the fracture walls.

**Keywords** Hydraulic properties · Fault zone · Crystalline rock · Permeability · BedrettoLab

## Eine multi-methodische Analyse der Permeabilitätsstruktur in spröden Störungszonen duktiler Einprägung im Kristallingestein

### Zusammenfassung

Spröde Störungen und Störungszonen gehören zu den hydraulisch aktivsten Elementen im überwiegend undurchlässigen Kristallingestein und stellen damit eine besondere Herausforderung für unterirdische Infrastrukturen wie Atommülllager dar. Spröde Störungszonen treten häufig entlang duktiler Scherzonen auf, die bereits bestehende Schwächezonen im Gestein darstellen.

---

✉ Julian Osten  
osten@lih.rwth-aachen.de

Tom Schaber  
schaber@lih.rwth-aachen.de

Garri Gaus  
garri.gaus@emr.rwth-aachen.de

Pooya Hamdi  
hamdi@lih.rwth-aachen.de

Florian Amann  
amann@lih.rwth-aachen.de

Peter Achtziger-Zupančič  
peter.achtziger-zupancic@ieg.fraunhofer.de

<sup>1</sup> Department of Engineering Geology and Hydrogeology, RWTH Aachen University, Lochnerstraße 4–20, 52064 Aachen, Germany

<sup>2</sup> Institute for Geology and Geochemistry of Petroleum and Coal, RWTH Aachen University, Lochnerstraße 4–20, 52064 Aachen, Germany

<sup>3</sup> Fraunhofer Research Institution for Energy Infrastructures and Geothermal Systems IEG, Kockerellstraße 17, 52062 Aachen, Germany

Vier spröde Störungszonen duktilen Ursprungs wurden im Rotondo-Granit vom „BedrettoLab“ in den Schweizer Zentralalpen analysiert. Scanline-Kartierungen, Gesteinsprobennahmen und Durchlässigkeitsmessungen mit drei verschiedenen Methoden liefern detaillierte Einblicke in die heterogene Störungszonenarchitektur und Hydrogeologie. Die durchschnittliche Permeabilität des intakten Gesteins liegt im Bereich von  $10^{-19}$  bis  $10^{-17}$  m<sup>2</sup>. Fließwege fokussieren sich auf einzelne offene oder teilweise mineralisierte Klüfte von punktuell bis zu  $10^{-14}$  m<sup>2</sup>, was durch selektive Messungen mit einem Gas-Permeameter und hydraulische Bohrlochtests gezeigt werden konnte. In unmittelbarer Nähe dieser durchlässigen Strukturen wurden verringerte Permeabilitäten gemessen, was auf Verwitterung in und um die Bruchwände hindeutet.

**Schlüsselwörter** Hydraulische Eigenschaften · Störungszone · Kristallingestein · Permeabilität · BedrettoLab

## Introduction

The German site selection law defines crystalline rock as a potential host rock for a radioactive waste repository. Of 90 sub-areas defined as having favorable geological conditions for the safe disposal of radioactive waste, 34% have crystalline rock as the target host rock (BGE 2020). Crystalline rock is or was considered as the potential host rock in other countries as well, such as Argentina, Canada, China, France, Great Britain, Japan, South Korea and Switzerland (Witherspoon and Bodvarsson 2006). Recently, in Olkiluoto (Finland) the first deep high-level radioactive waste facility was excavated in high-grade metamorphic to magmatic paragneisses and granitoids (Aaltonen et al. 2016).

Water flow and associated radionuclide transport in crystalline rock is mostly focused in brittle fault zones, faults and fracture zones (e.g. Bense et al. 2013; Faulkner et al. 2010; Achtziger-Zupančič et al. 2016; Tsang et al. 2015). In crystalline rock, brittle fault zones often occur along ductile shear zones (Wehrens et al. 2017; Aaltonen et al. 2016; Drake et al. 2006; Lützenkirchen and Loew 2011; Tourigny and Tremblay 1997), which typically develop at depths > 10–15 km and at temperatures > 250–350 °C (Sibson 1977). Ductile shear zones are characterized by accumulations of pervasive foliation defined by phyllosilicates and by grain size reduction, both introducing a mechanical contrast prone for reactivation as brittle fault zones during exhumation if oriented preferably in the governing stress field (Tourigny and Tremblay 1997; Stenval et al. 2019; Shea and Kronenberg 1993). In the brittle regime, strain accumulates along discrete fractures at both the grain and macroscale (Sibson 1983), defined as faults. Rock volumes in the domain of one or more subparallel faults that contain smaller fractures and faults, fault rock assemblages and subsidiary deformation structures constitute fault zones (Choi et al. 2016). Following the conceptual model of Caine et al. (1996), fault zones can be divided into a fault core, where most of the strain is accommodated and a damage zone formed by a network of smaller faults and joints. Depending on the distribution and hydraulic properties of these structural elements, fault zones can act as conduits, barriers, or a combination of both. Faulkner et al. (2003) expanded

this simple model for more complex fault zones consisting of several anastomosing fault core strands around lenses of variably fractured protolith. As granitoids are rocks with a primary matrix porosity of < 1% (Géraud et al. 1995; Wenning et al. 2018; Möri et al. 2021; Drake et al. 2006; Aaltonen et al. 2016), they are associated with a low matrix permeability of <  $10^{-19}$  m<sup>2</sup> (Wenning et al. 2018; Brixel et al. 2020; Achtziger-Zupančič et al. 2017; Scibek 2019; Snowdon et al. 2021; Tsang et al. 2015). Fault core permeability is mostly gouge controlled and might be less than the matrix permeability, whereas the damage zone permeability is controlled by a network of partially mineralized and open fractures, commonly exceeding the intact rock permeability.

Preferential flow paths are mostly observed along fractures undergoing shearing or dilation in the respective stress field (Sibson 1977; Tourigny and Tremblay 1997; Achtziger-Zupančič et al. 2016; Faulkner et al. 2010; Bense et al. 2013). These structures may promote upwelling of highly mineralized thermal fluids, coating and partially closing fractures with accessory minerals when cooled (Michibayashi et al. 1999; Kluge et al. 2021; Aaltonen et al. 2016; Drake et al. 2006; Tourigny and Tremblay 1997; Lützenkirchen and Loew 2011). The resulting reduction in porosity and connectivity leads to further channeling of fluid flow towards the remaining (partially) open fractures (Brixel et al. 2020; Wenning et al. 2018). The combination of ductile and brittle deformation structures, partially altered by hydrothermal fluids, imposes hydraulic complexity in granitoidic rocks. To assess the interaction of the different fault components, the permeability of the ductile and brittle deformed Rotondo Granite at the Bedretto Tunnel was tested using three different methods, each addressing a different scale and test volume. Centimeter-scale pulse decay tests in a triaxial flow cell were used to provide an average bulk permeability, and small-scale packer tests (0.2 to 1 m intervals) in boreholes provided average flow permeabilities. A gas probe permeameter developed by Scibek and Annesley (2021), used to measure point-scale permeability, was able to cover the range in scale between flow cell and borehole tests. The combination of the different methods shows an anisotropic permeability distribution that

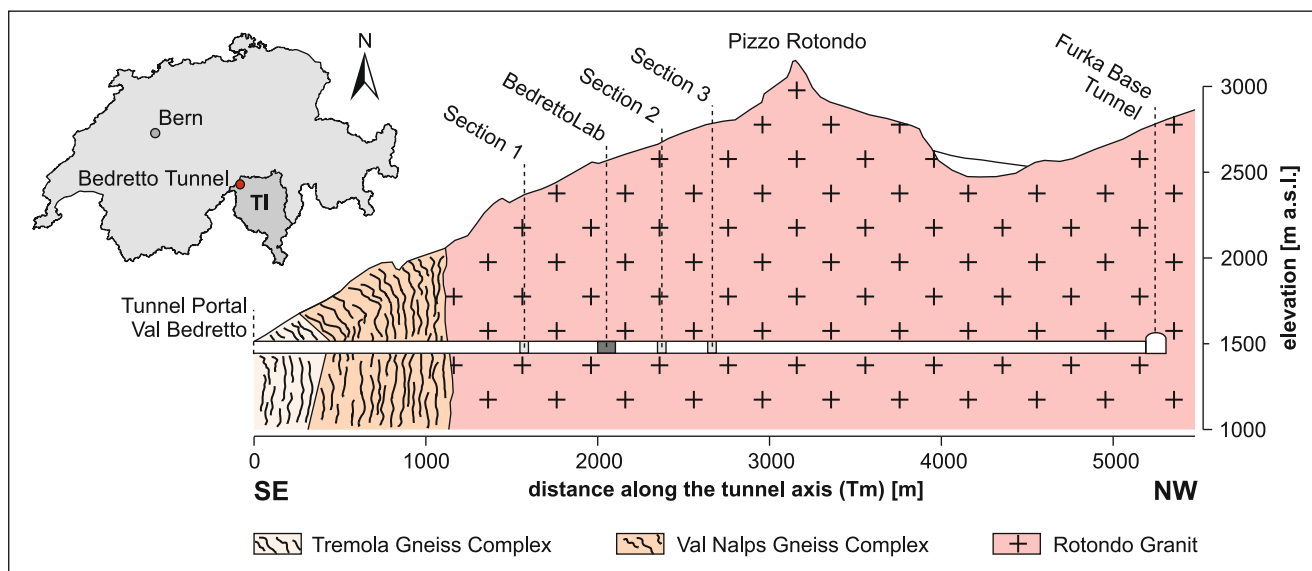


**Fig. 1** Location of the Bedretto Tunnel in the Canton of Ticino (TI), Switzerland, and simplified cross-section showing lithologies, the investigated tunnel sections and the BedrettoLab, modified after Keller and Schneider (1982) and Rast et al. (2022). [a.s.l.]: above sea level

**Abb. 1** Lage des Bedretto-Tunnels im Tessin (TI), Schweiz und vereinfachter Querschnitt mit Darstellung der Lithologien, der untersuchten Tunnelabschnitte und des BedrettoLabors, modifiziert nach Keller und Schneider (1982) und Rast et al. (2022). [a.s.l.]: über dem Meeresspiegel

is primarily controlled by the structural geology. Fluid flow is concentrated in single flow paths along partially open fractures, while mineral-filled fractures have similar low permeability as the matrix. A large permeability contrast is often found within a few centimeters.

## Background and geology

### Bedretto Tunnel

The 5218 m long Bedretto Tunnel in the Swiss Central Alps was excavated by drill and blast between 1971 and 1982 to accelerate the transport of excavated material from the Furka Base Tunnel construction to Val Bedretto (Amberg 1982). In 2019, ETH Zürich established the “Bedretto Underground Lab for Geosciences and Geoenergies” (BULGG) in the tunnel, to host experiments on deep underground stimulation in the context of geothermal energy and earthquake prediction (Ma et al. 2022; Gischig et al. 2020). The mostly unlined tunnel was made accessible along its entire length, providing unique insights into the composition and structure of the adjacent rock mass.

The Bedretto Tunnel crosses three lithostratigraphic units of the Gotthard Nappe. Pre- and early-Variscan gneisses, schists and amphibolites of the Tremola Gneiss Complex and the Val Nalps Gneiss Complex are found in the southern part of the tunnel while the major portion of the Bedretto Tunnel passes through the late Variscan Rotondo Granite (Berger et al. 2017; Labhart 1975). Locations in the

Bedretto Tunnel are given in “Tm”, referring to the tunnel meter range from Tm 0 at the at the Ronco tunnel portal in Val Bedretto in the SE to Tm 5218 at the conjunction with the Furka Base Tunnel in the NW (Fig. 1).

### Rotondo Granite

The Rotondo Granite is a late to post-Variscan intrusion of the Gotthard Nappe in the Swiss Central Alps, mostly outcropping in the mountain range north of Val Bedretto and in the Bedretto Tunnel from Tm 1138 to its NW end. The light-grey, fine- to medium-grained granite is composed mainly of quartz, alkali feldspar, plagioclase and biotite with minor fractions of garnet, phengite, chlorite, epidote, apatite and zircon (Labhart 1975). It shows evidence of ductile deformation by pervasive foliation defined by biotite and reduced grain sizes that accumulate around ductile shear zones.

Rast et al. (2022) distinguished two different types of shear zones. Granitic shear zones with a mineralogical composition similar to that of the surrounding rock occur throughout the entire Bedretto Tunnel, whereas quartz- and biotite-enriched shear zones are restricted to the rear part of the tunnel beyond Tm 2800. The two types of shear zones localized strain during ductile deformation along rheological contacts in the granite and mechanically weaker mafic intrusions, respectively (Rast et al. 2022).

The Rotondo Granite exhibits brittle faults and fault zones of varying sizes, ranging from a few centimeters to several meters. Brittle fault zones beyond Tm 3775, which were analyzed by Lützenkirchen and Loew (2011)

are mostly situated entirely within ductile shear zones, while a smaller number of fault zones exhibit damage zones exceeding the extent of ductile shear zones or do not show evidence of any ductile deformation. Fault zones can be grouped by their orientation in four clusters (Ma et al. 2022; Jordan 2019). The most numerous cluster consists of sub-vertical structures striking WSW-ENE to SW-NE.

This study focuses on three locations in the Bedretto Tunnel (Sects. 1, 2 and 3, Fig. 1) with 800–1200 m of overburden, where variably sized and tectonically deformed fault zones and their hydraulic characteristics are described in detail.

## Methods

### Scanline mapping, drilling and sample preparation

Scanline mapping was conducted according to the International Standard for Rock Mechanics (ISRM 1978) to assess the structure and composition of the Rotondo Granite. A measuring tape was installed along the tunnel sidewall and all discontinuities crossing the measuring tape were identified and their characteristics (i.e. orientation, persistence, aperture) recorded.

In Sects. 1 and 2, eight short (<1 m) 56 mm diameter boreholes were drilled sub-horizontally into the tunnel wall. A total of 11 cylindrical samples of 38 mm diameter and 43 to 80 cm in length, were extracted from the core by sawing and overcoring. These samples were used for porosity, density, hydraulic flow cell and gas probe permeameter measurements. In Sect. 3, three parallel, 76 mm diameter, 10–11 m long boreholes (BRI\_A\_01 to BRI\_A\_03) were drilled sub-horizontally, approximately perpendicular to the SW-wall of the Bedretto Tunnel. The borehole spacing is 2 m. Representative sections of the drill cores were chosen to undertake gas probe permeameter measurements and in-situ borehole hydraulic testing. Since there was virtually no core loss, the most disturbed zones could also be sampled.

### Porosity and density

Connected porosity and dry bulk density  $Q_d$  were determined using standard saturation and buoyancy techniques (ISRM 1979). The grain density of finely ground rock powder  $Q_{gr}$  was measured in a He-pycnometer. The total porosity, comprising connected and unconnected pores, was calculated as  $1 - (Q_d/Q_{gr})$ .

### Pressure-decay gas probe permeameter

A pressure-decay gas probe permeameter using air (Scibek and Annesley 2021) was used to assess point permeability

(Fig. 2a, b). A rubber seal tip, connected to an upstream gas reservoir is pressed against a ~1 cm diameter epoxy resin ring glued on the desired spot on the test surface. The reservoir pressure is generated by a manual air pump or a compressor and measured by a pressure transducer (Keller Series 33X). The initial upstream reservoir pressure prior to measurements is set to approximately 0.3 MPa to avoid mechanical effects and leakage. The average measurement time is 25 to 30 min. Permeability is related to the pressure decay as described in Scibek and Annesley (2021), assuming flow through fractured media to concur with Darcy's law. The gas probe permeameter measures small test volumes that show a large scatter for different rock structures.

Therefore, test spots and associated permeabilities were categorized into (1) rock matrix without visible damage structures, (2) partially open fractures, defined by a visible aperture in their trace, (3) mineral-filled (healed) fractures, and (4) hydro-thermally altered quartz-feldspar veins as observed in cores from Sect. 3. A minimum of two tests have been conducted on the top, bottom and circumference of the samples from Sect. 1, also used in flow cell tests.

### Hydraulic flow cell permeability

Stress-dependent permeability of cm-scale cylindrical rock samples was assessed following the methodology described by Brace et al. (1968), whereby the setup and implementation were similar to those of David et al. (2020), who measured the permeability of macroscopically unfractured Rotondo Granite.

The experimental setup is shown in Fig. 2c. A cylindrical rock sample is placed between two pistons with water inlets. Porous steel discs are placed between the sample and the pistons to ensure uniform fluid distribution. Sample, steel discs, and parts of the pistons are jacketed by a heat shrink tube, and placed into a hollow steel cylinder. O-rings seal the space between the pistons and the hollow cylinder, which is filled with water acting as confining fluid with pressure  $P_{conf}$ . An axial load  $F_a$ , corresponding to  $P_{conf}$  is applied to ensure hydrostatic stress conditions. The sample is connected to two calibrated volumes. The upstream pressure  $P_{up}$  and the downstream pressure  $P_{down}$  are recorded by pressure sensors (Keller Series 33X) at a rate of 1 Hz. Valves V1, V2 and V3 control the connection of the reservoirs to each other and to a water pump or vacuum pump. Permeability was measured at 5, 10, 15 and 20 MPa confining pressure on samples from Sect. 1 and at 5 and 20 MPa confining pressure on samples from Sect. 2. After slowly increasing  $F_a$  and  $P_{conf}$  to the targeted stress, the valves are opened and the entire system evacuated. A constant water pore pressure  $P_p$  of 2 MPa is then applied for at least 48 h to ensure water saturation of the sample. Subsequently, the

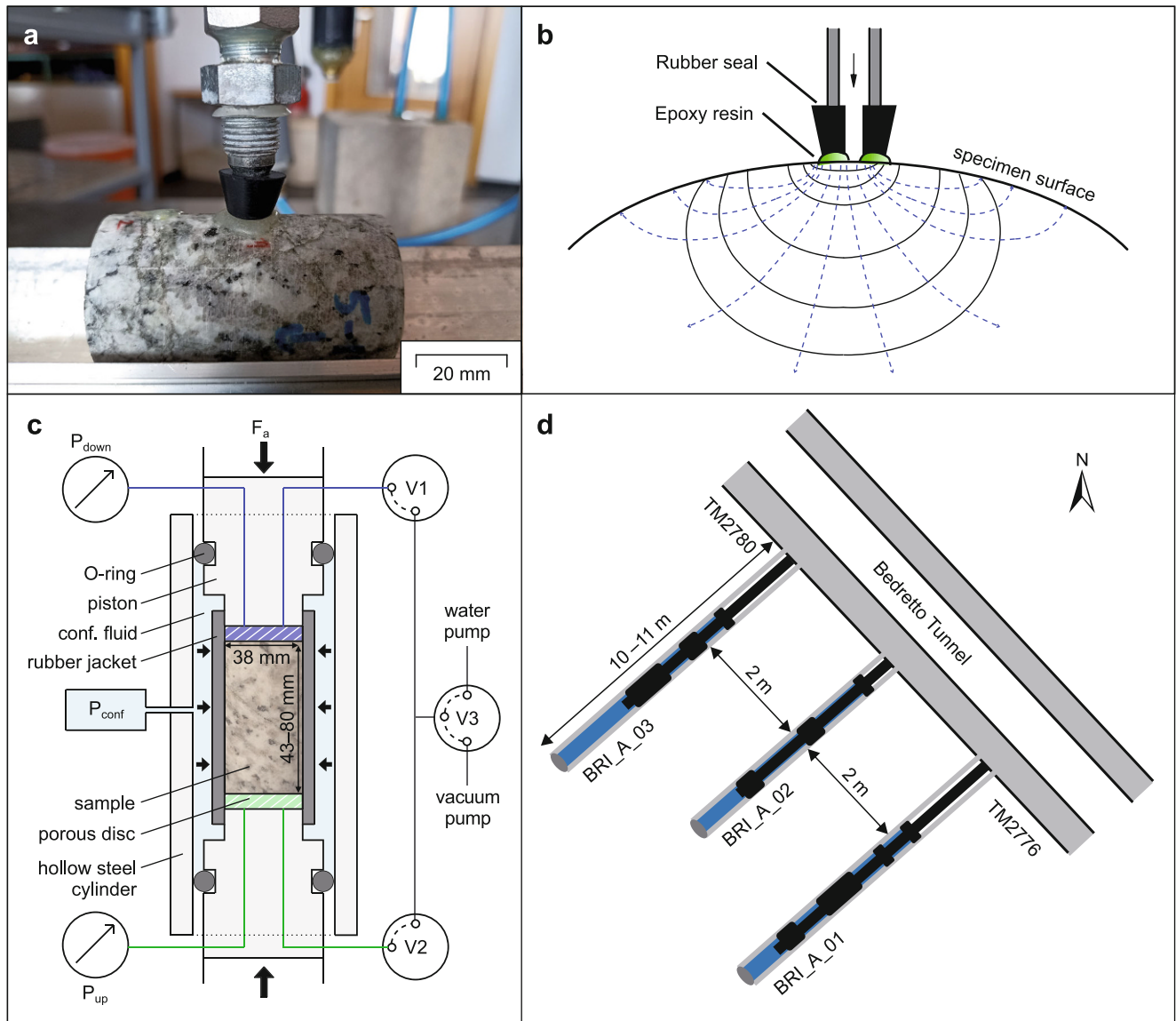


**Fig. 2** Methods for permeability measurement: **a, b** rubber tip of the gas probe permeameter pressed against the epoxy ring on a sample, modified after Scibek and Annesley (2021), **c** schematic of the triaxial flow cell setup, upstream reservoir in green and downstream reservoir in blue, **d** schematic of the hydraulic borehole test setup, top view

**Abb. 2** Methoden zur Permeabilitätsmessung: **a, b** Gummispitze des Gaspermeameters, die gegen den Epoxidring auf einer Probe gedrückt wird, modifiziert nach Scibek und Annesley (2021), **c** Schema des triaxialen Durchflusszellenaufbaus, stromaufwärts gelegenes Reservoir in grün und stromabwärts gelegenes Reservoir in blau, **d** Schema des hydraulischen Bohrlochtestaufbaus, Draufsicht

valves are closed and the pump pressure is increased by 0.5 MPa. A pressure pulse of 0.5 MPa is induced on the upstream side of the sample by shortly (~1 s) opening valve V1.

Pressure decay of  $P_{up}$  and pressure rise of  $P_{down}$  are recorded until both reservoirs are equilibrated to a final pressure. Finally, the initial pore pressure of 2 MPa is restored. At least two measurements are taken at each stress level. The effective stress on the sample is defined as  $P_{conf} - P_p$ .

**Borehole hydraulic tests**

In-situ hydraulic permeability of Rotondo Granite is assessed in three sub-horizontal (5° to 10° dip) boreholes of 76 mm diameter which have been equipped with modular multi-packer systems, isolating borehole sections of 0.2, 0.5 and 1 m length (Fig. 2d). Packer sleeve lengths are 0.25, 0.5 and 1 m. Various tests including constant rate, constant head and pulse injection tests are conducted in the isolated sections. A single interval showed sufficient productivity for withdrawal tests (3.3 ml/min). Pressures and flow rates are

monitored by an uphole data acquisition system mounted onto a testing trailer. The setup allows to measure pressures of up to 10 MPa and water flow rates between 0.017 and 660 ml/min with a frequency of 1 Hz. The maximum difference in test pressure was usually kept below 0.3 MPa.

The recovery phase after a hydraulic pulse test is analyzed by type curve matching (Bredehoeft and Papadopoulos 1980; Cooper Jr. et al. 1967). Constant head/rate tests are separated into the active flow phase and the pressure recovery phase, which are analyzed by diagnostic plots and straight-line analysis (Cooper Jr. and Jacob 1946; Jacob and Lohman 1952; Theis 1935; Horner 1951). Hydraulic conductivity is recalculated to permeability, using tabulated dynamic viscosity and water density at atmospheric pressure and a measured water temperature of about 17.5 °C.

## Results

### Section 1: Tm 1583–Tm 1592

In Sect. 1, a well-developed E-W striking and steeply N-dipping fault zone crops out between Tm 1583 and Tm 1592 on the NE wall and between Tm 1586 and Tm 1595 on the SE wall of the Bedretto Tunnel. Surrounded by massive sections of Rotondo Granite, the fracture frequency gradually increases towards the fault zone center, which is characterized by anastomosing, a few centimeter-thick bands of intensively foliated rock, partially altered into incohesive gouge. They are accompanied by similarly thick quartz veins separating lenses of heavily fractured, partially brecciated granite (Fig. 3a).

Four short (<1 m) subhorizontal boreholes were drilled in Sect. 1. The locations of boreholes BH02, BH03 and BH04 on the SW-wall are shown in Fig. 3c, another borehole BH01 was drilled into the opposite NW-wall. Six 43–80 cm long cylindrical rock samples of 38 mm diameter were extracted to determine density, porosity and permeability.

The average connected porosity is  $1.03 \pm 0.06\%$  and the average total porosity is  $2.6 \pm 0.2\%$  based on a grain density of  $2659 \pm 3 \text{ kg/m}^3$ . The average dry bulk density is  $2590 \pm 6 \text{ kg/m}^3$ . Hydraulic flow cell permeability measured for five samples under 3, 8, 13 and 18 MPa effective stress ranges from  $8 \cdot 10^{-20}$  to  $2 \cdot 10^{-18} \text{ m}^2$ . Apart from one sample that was excluded from further analysis, permeability decreases at higher confinement levels, roughly following an exponential relationship, comparable to Marschall and Lunati (2006). Gas probe permeability measured on 31 spots on the same cylindrical samples varies from  $2 \cdot 10^{-18}$  to  $3 \cdot 10^{-15} \text{ m}^2$ , the highest permeability measured for an open fracture.

Permeability measured on rock samples from BH03 and BH04 is shown in Fig. 3a. Measurement locations were pro-

jected from the borehole location onto the scanline along the tunnel wall. A large variability in permeability was observed for test spots of close proximity. Higher permeabilities are concentrated around the high strain quartz vein near the center of the fault zone, close to the highest fracture density. Fracture density and permeability increase from the protolith towards the borders of the fault zone center. Within the center, fracture density and permeability are variable and tend to be decreased again.

### Section 2: Tm 2376–Tm 2386

Section 2 is situated at the SW-wall of the Bedretto Tunnel between Tm 2376 and Tm 2386. A scanline survey indicates 5 intervals with a very high degree of fracturing separated by slightly more intact but still damaged rock portions within the 10 m interval. Approximately WSW-ENE striking fractures and faults are clustered at 2 positions, with a spacing of roughly 7 m. The volume between the main fault planes is more intensely fractured rock mass. At the NW-wall, a third major fault plane is observed. These three faults, dipping roughly 60–70° towards the NNW, show accumulations of foliation and reduced grains resulting in bands of darker appearance. White gouge, consisting of quartz-rich rock fragments, phyllosilicates and zeolites (Volpe et al. 2023), is distributed in patches of usually less than 1 cm normal thickness in some main faults, comparable to observations in other faults as described in Lützenkirchen and Loew (2011). The fault zone is larger with more separate main fault plains, but exhibits some similarities to Sect. 1 with respect to the distribution of quartz veins along bands of strongly foliated and partially altered granite, in this case in a repetitive sequence.

The average connected porosity for five 44–72 cm long cylindrical rock samples is  $0.98 \pm 0.08\%$  and the average total porosity is  $2.1 \pm 0.2\%$ . The average dry bulk density is  $2604 \pm 4 \text{ kg/m}^3$ . Hydraulic flow cell permeability, measured for five samples under 3 and 18 MPa effective stress ranges from 1 to  $6 \cdot 10^{-19} \text{ m}^2$ , which is in a similar range compared to Sect. 1 with less scatter. Under the assumption of the same exponential relation as observed in Sect. 1, results were also extrapolated to 0 MPa effective stress. Gas probe permeability measured on 33 spots on the same samples varies from  $10^{-18} \text{ m}^2$  to  $9 \cdot 10^{-14} \text{ m}^2$ . Overall, similar results as in Sect. 1 are observed with high permeability differences over relatively short distances, e.g.  $4 \cdot 10^{-14} \text{ m}^2$  and  $10^{-17} \text{ m}^2$  within a few millimeters, highest permeabilities in open fractures, and roughly similar values for matrix and healed fractures. Given the width of the fault zone and the few short samples tested, clear dependencies between permeability and fracture distribution are not seen.

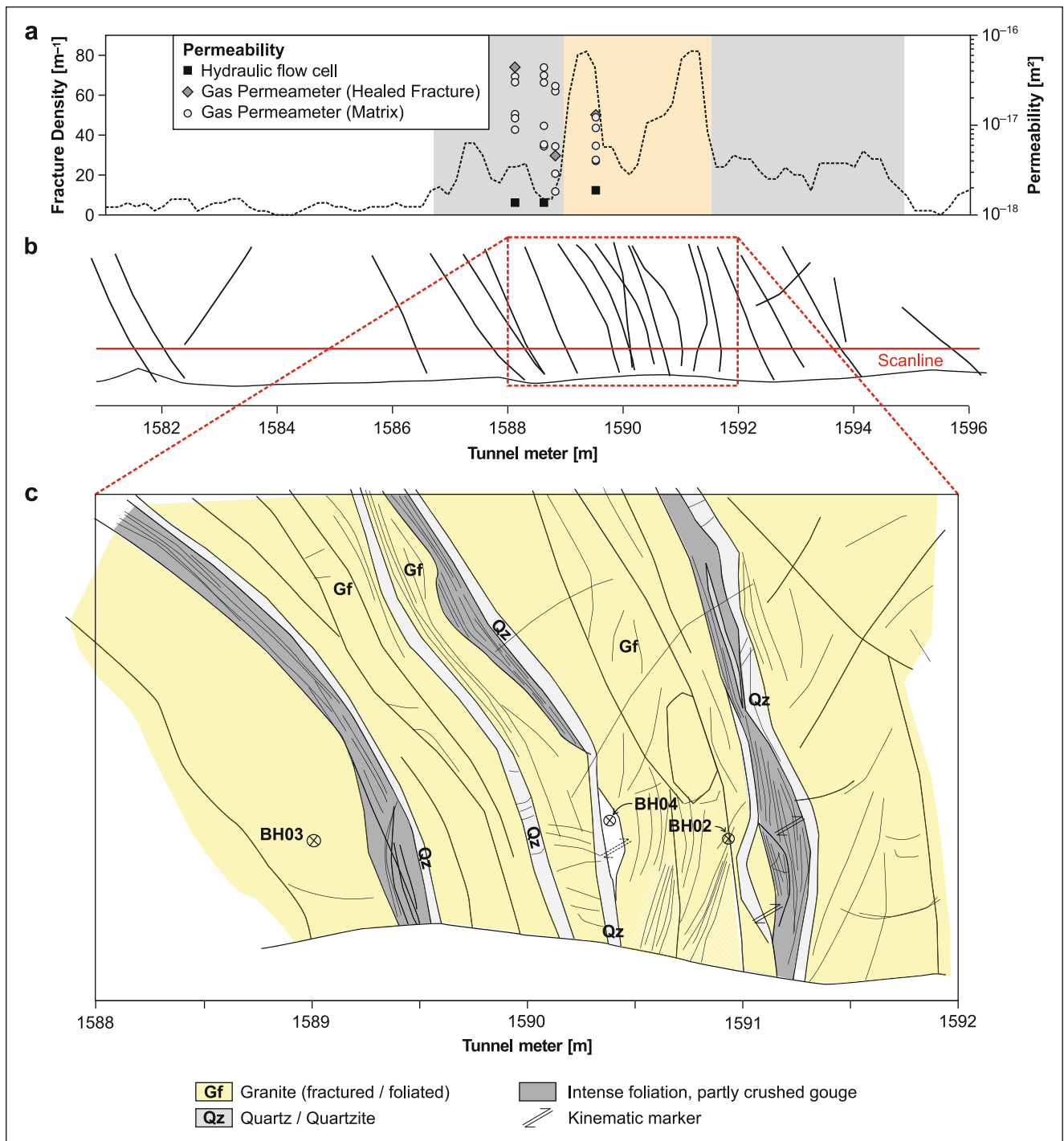


**Fig. 3** Section 1: **a** Fracture density measured along the SW-face of the Bedretto Tunnel and permeability determined by the gas probe permeameter and the hydraulic flow cell extrapolated to 0MPa effective stress. The highest permeability of  $2 \cdot 10^{-14} m^2$  was measured in a partially open fracture at the opposite tunnel wall. The grey area shows the damage zone and the orange area highly fractured domains around the fault core, determined according to Torabi et al. (2020); **b** Rough sketch of the SW-tunnel wall at Sect. 1 with major fractures and faults and location of the scanline used for mapping; **c** Detailed sketch of the fault zone center in Sect. 1 and locations of short boreholes BH01–BH03

**Abb. 3** Abschnitt 1: **a** Entlang der SW-Seite des Bedretto-Tunnels gemessene Kluftdichte und die mit dem Gaspermeameter und der hydraulischen Durchflusszelle ermittelte Permeabilität, extrapoliert auf 0MPa effektive Spannung. Die höchste Durchlässigkeit von  $2 \cdot 10^{-14} m^2$  wurde in einem teilweise offenen Bruch an der gegenüberliegenden Tunnelwand gemessen. Der graue Bereich zeigt die Auflockerungszone und der orangefarbene Bereich die stark geklüfteten Bereiche um den Störungskern, die nach Torabi et al. (2020) bestimmt wurden; **b** Grobe Skizze der SW-Tunnelwand in Abschn. 1 mit den wichtigsten Klüften und Störungen und der Lage des für die Kartierung verwendeten Scanline; **c** detaillierte Skizze des Störungszentrums in Abschn. 1 und der Lage der kurzen Bohrlöcher BH01–BH03

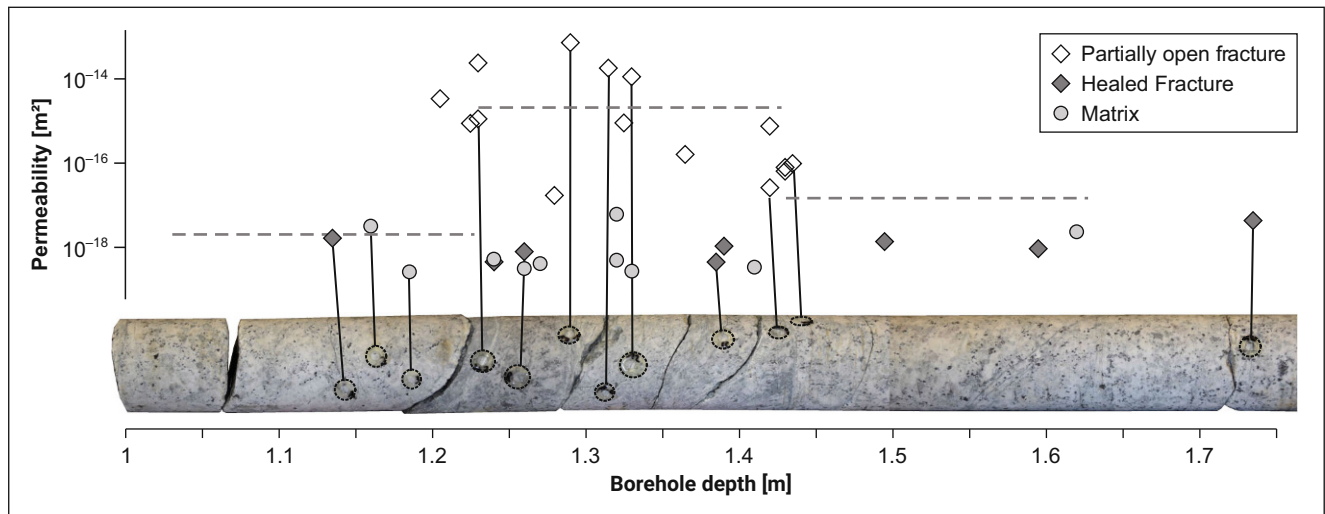


**Fig. 4** Fault zone section in borehole BRI\_A\_01 drilled into the SW wall of the Bedretto Tunnel at Tm 2776, permeability measured by hydraulic borehole tests in the corresponding borehole interval (*dashed lines*) and the gas probe permeameter assigned to different spots along the core. Unassigned values were measured on the opposite side of the core (not shown)

**Abb. 4** Störungszonenabschnitt im Bohrloch BRI\_A\_01, der in der SW-Wand des Bedrettotunnels bei Tm 2776 erbohrt wurde, sowie die mit hydraulischen Bohrlochtests gemessene Durchlässigkeit im entsprechenden Bohrlochintervall (*gestrichelte Linien*) zusammen mit den Gaspermeameter Ergebnissen entlang des Kerns. Nicht zugeordnete Werte wurden auf der gegenüberliegenden Seite des Kerns gemessen (nicht dargestellt)

### Section 3: Tm 2765–Tm 2780

Section 3 is located between Tm 2770 and Tm 2780, where three 10–11 m long boreholes were drilled perpendicularly into the SW tunnel wall (Fig. 2d). The drill holes were logged using an optical televiewer (OpTV). Detailed scan-line mapping and core logging surveys were also performed in this area.

Two major structures are observable at the tunnel wall and can be correlated through the cores. A structure outcropping along the SW-wall between Tm 2764 and Tm 2767.5 is up to 1 m wide and dipping about 60° towards the WSW. The structure is well-exposed at the tunnel roof for a few decameters of trace length and up to 5 fractures striking sub-parallel to the tunnel were mapped from the OpTV surveys between 1 and 3 m in all three boreholes. As observed in the cores at similar positions and at the tunnel wall and roof, the fault zone consists of biotite-rich anastomosing rims, sandwiching brecciated and sheared quartz-feldspar bands and partially brecciated lenses of wall rock. The fracture network is mineral-filled with a silica-rich glassy matrix and altered green-grey chlorite, both likely of hydro-thermal origin.

The second fault outcropping between Tm 2772.3 and Tm 2773.9 at the SW-wall is about 0.5 m wide and dipping 75° to 80° towards the NNE. The main part of the structure is characterized by a roughly 0.3 m thick, coarse grained quartz-feldspar vein with a sharp contact to a heterogeneous fracture network, consisting of open fractures, healed fractures, and a generally variable texture. In borehole BRI\_A\_03 only two chlorite-coated fractures are ob-

served, accompanied with reoriented coarse-grained quartz and feldspar.

A total of 118 single gas probe permeameter measurements have been conducted on the cores with gas permeability ranging from  $2 \cdot 10^{-19} \text{ m}^2$  to  $8 \cdot 10^{-14} \text{ m}^2$ . Results of the extensively tested core section of BRI\_A\_01 between 1 and 1.75 m depth are shown in Fig. 4. The interval covers the intersection of the two fault structures described above. A central section, found between 1.2 and 1.35 m is characterized by several partially open fractures of permeabilities up to  $7 \cdot 10^{-14} \text{ m}^2$ , while adjacent mineral-filled fractures and matrix have permeabilities similar to the undamaged domains of Rotondo Granite ( $10^{-18} \text{ m}^2$ ). Fractured quartz-feldspar-veins in other borehole sections show variable permeabilities whereas matrix and healed fracture permeabilities are in the same range. Like in Sects. 1 and 2, high and low permeability values are observed in close proximity. Filled fractures within damaged core intervals tend to show even lower permeability compared to the matrix.

18 packed-off intervals were tested in the boreholes BRI\_A\_01 to BRI\_A\_03 beyond 0.7 m borehole depth to avoid the influence of the excavation damage zone (EDZ). A total of 22 analyzable hydraulic pulse tests, 2 hydraulic constant head/flow tests and 1 withdrawal test are included in this analysis. Some constant rate/head tests showed multiple hydraulic phases, which were analyzed as separate tests, resulting in a total of 33 single permeability values. Permeabilities vary between  $10^{-19} \text{ m}^2$  and  $2 \cdot 10^{-15} \text{ m}^2$ . The difference between maximum and minimum permeabilities in a single sequence of tests rarely exceeds a factor 5. In intervals incorporating brittle structures as determined visu-



ally or by OpTV logs, hydraulic tests consistently showed values higher than  $10^{-16} \text{ m}^2$  (e.g. Fig. 4).

## Discussion

### Comparison of the methods

Distribution of permeabilities measured by the gas probe permeameter for different rock structures, by the flow cell and by borehole hydraulic testing, are compared in Fig. 5a. Flow cell results are extrapolated to 0MPa effective stress in a  $P_{eff}\text{-log(permeability)}$  plot to ensure comparability with permeabilities resulting from the other methods. Borehole packer intervals analyzed with multiple tests or phases were averaged. Gas probe permeameter measurements conducted at Sects. 1 and 2 coincide with results from Sect. 3 and are therefore displayed together. Gas probe permeability is assumed to be overestimated due to the gas slippage effect (Klinkenberg 1941). However, gas permeability was not Klinkenberg corrected since (1) permeability was measured for a small range of pore pressures, preventing the direct determination of the Klinkenberg gas slippage coefficient and (2) a lack of empirical correlations for the gas slippage correction in (fractured) granitoidic rocks. Studies on porous sandstones (Tanikawa and Shimamoto 2009) indicate 2–3 times lower water permeability for gas permeability in the range of  $10^{-18}$  to  $10^{-17} \text{ m}^2$  for the pore pressure of 0.3MPa used in this study. For higher permeabilities, the gas-slippage effect is further reduced. Rock properties from locations that are close to the walls of the drill and blast tunnel, such as samples from Sects. 1 and 2, might be affected by excavation damage. Hardenbicker (2023) estimated an excavation damage zone of 0.5 to 0.7m in the Rotondo Granite of the Bedretto Tunnel. However, this is not expected to have a significant effect on the measurements as there is evidence of spalling of EDZ-affected rock material in and around the fault zones crossing the tunnel. Thus, the influence of the fault structures is expected to be greater than that of the EDZ.

The gas probe permeameter measurements, covering a small rock volume of a few  $\text{cm}^3$ , allow to test selective features separately on a local scale to detect spatial relations on very short distances. The influenced volume varies strongly with the permeability of the tested feature as evidenced by bubble tracing during the tests. Given the high variability of structural features and small scale of measurements, gas probe permeameter tests yield the largest permeability variation in the range of  $2 \cdot 10^{-19} \text{ m}^2$  to  $9 \cdot 10^{-14}$ . The permeability of mineral-filled fractures and the rock matrix does not differ recognizably and is similarly low. The quartz-feldspar veins show greater scatter and higher overall permeability, suggesting a heterogeneous perme-

ability distribution in these domains. Testing partially open fractures allows to target preferential flow channels, which may be primary contributors to the fault zone permeability.

These channels, albeit more difficult to target individually, are expected to be the main permeability contributors in hydraulic borehole tests. Borehole tests cover larger test volumes of up to a few cubic meters, depending on the interval length, test duration and the permeability of the most conductive structures within the interval. The results, spanning from  $10^{-19} \text{ m}^2$  to  $2 \cdot 10^{-15} \text{ m}^2$  for individual tests, exhibit a narrower range than the gas probe permeameter measurements. This suggests the presence of an averaging effect over the tested interval (Fig. 5a). The borehole test results agree with the log-mean of open fractures measured in gas probe permeameter tests conducted on cores from the same interval (compare Fig. 4).

Hydraulic flow cell measurements cover the test volume of the respective rock cylinders from  $50 \text{ cm}^3$  to  $90 \text{ cm}^3$ . Permeability, extrapolated to 0MPa effective stress, is between  $2 \cdot 10^{-19} \text{ m}^2$  and  $2 \cdot 10^{-18} \text{ m}^2$ , which is lower and less variable than results of the other two methods. Although the samples originate from zones of increased damage in the fault zone and exhibit healed and partly open fractures, no correlation between macroscopic deformation and flow cell permeability is observed, suggesting that preferential flow paths are missed. Bubble tracing during gas probe permeameter tests indicates flow channels predominantly in macroscopic visual open and mineral-filled fractures but only small parts of the fracture planes tend to act as a conduit whereas a large portion may act as barrier. The gas probe permeameter can selectively target highly conductive channels whereas the borehole measurements are expected to test averages over fractures and matrix and to show the effects of connectivity of small-scale fracture permeability. However, yielding similar observations by the hydraulic flow cell test requires the abundant permeable fractures to be oriented sub-parallel to the sample axis. Otherwise, flow-cell measurements may represent a minimum estimate of bulk permeability of the Rotondo Granite. In contrast to the other methods measured under in-situ conditions or atmospheric pressure, the hydraulic flow cell allows for the adjustment of confining stress. Flow cell permeability of the Rotondo Granite decreases by 22 to 71% from 3MPa to 18MPa effective stress. Measured permeability is slightly lower compared to results by David et al. (2020) on macroscopically unfractured Rotondo Granite.

In conclusion, flow cell measurements can provide an average bulk permeability and borehole hydraulic tests can provide a mean flow permeability. Gas probe permeameter tests are able to cover the range in between and allow to estimate local variability. However, the uncertainty of this measurement type is high due to frequent unknown representativity of the test spot area and the insufficiently

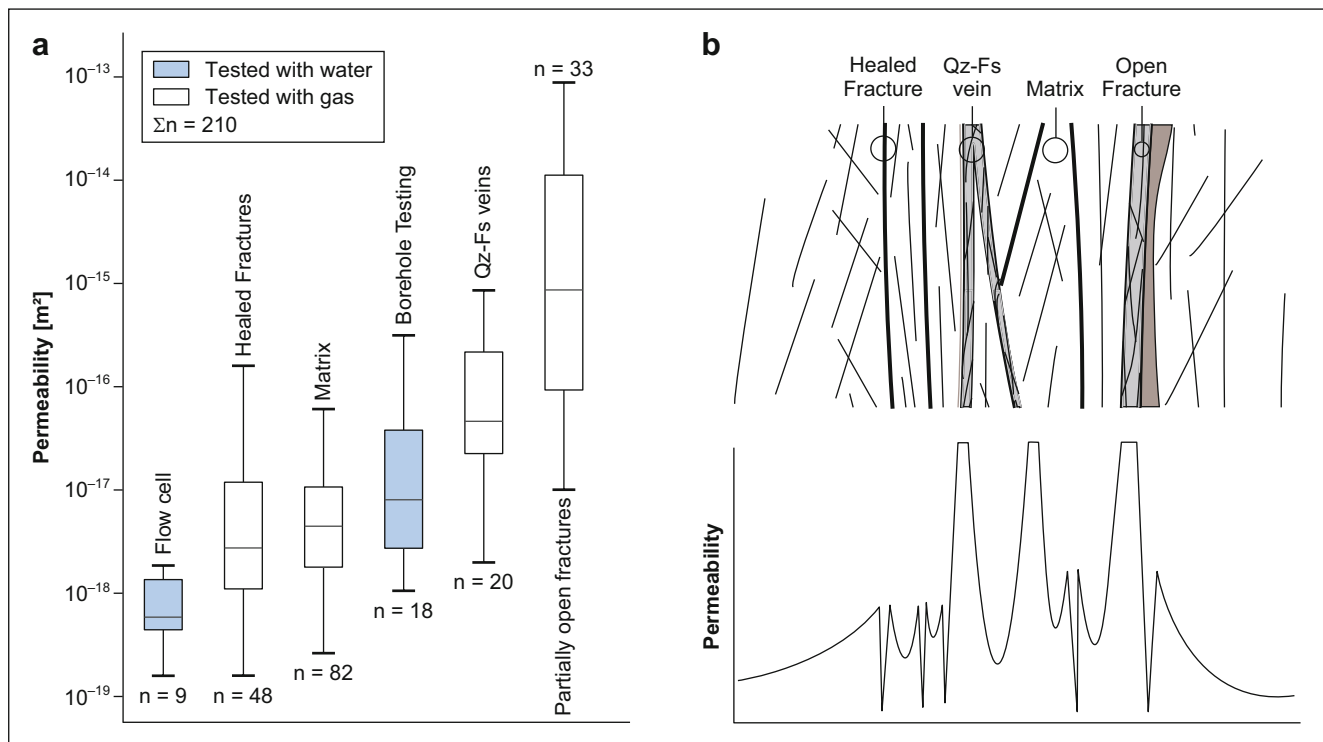


**Fig. 5** **a** Distribution of the gas probe permeameter results with respect to the structural element of the fault zone and in comparison, to the flow cell results extrapolated to 0MPa effective stress and borehole hydraulic measurements. Note that the data are not necessarily normal distributed. **b** Resulting hydro-structural model of brittle overprinted ductile shear zones, modified after Faulkner et al. (2010). Note that the model is dimensionless as thicker structures are “self-similar” repetitions of smaller ones

**Abb. 5** **a** Verteilung der Ergebnisse des Gaspermeameters in Bezug auf die Strukturelemente der Störungszone und im Vergleich zu den auf 0MPa effektive Spannung extrapolierten Ergebnissen der Fließzelle und der hydraulischen Bohrlochmessungen. Es ist zu beachten, dass die einzelnen Daten nicht notwendigerweise normalverteilt sind. **b** Resultierendes hydrostrukturelles Modell von spröde-überprägten duktilen Scherzonen, modifiziert nach Faulkner et al. (2010). Das Modell ist dimensionslos; dickere Strukturen können „selbstähnliche“ Wiederholungen von kleineren Strukturen darstellen

researched effect of the test fluid on the test result. Absolute values should be taken with care but measurements can be compared relatively to each other. The described scale effects are well known and are attributed to the sample selection, the test volume and statistical effects (e.g. Clauser 1992; Illman 2006).

### Permeability structure of the Bedretto fault zones

Four fault zones of variable size and orientation have been investigated in three sections of the Bedretto Tunnel. They share the general development from a ductile imprinted mechanical anisotropy caused by grain size reduction and foliation. Fractured and brecciated granite lenses are aligned or sandwiched by a single or multiple main fault planes which developed along foliated, biotite-rich bands. Around these faults a damage zone may occur or may be absent. The parts of the fault zone are connected through partially healed or open fractures.

Comparable structures are frequent in the Rotondo Granite (Lützenkirchen and Loew 2011; Jordan 2019; Rast et al.

2022), in the alpine external massifs (Wehrens et al. 2017) and elsewhere (e.g. Aaltonen et al. 2016; Drake et al. 2006; Michibayashi et al. 1999; Vauchez 1987). The development from ductile shear zones to brittle fault zones was also frequently observed (Vauchez 1987; Herwegh et al. 2017; Lützenkirchen and Loew 2011). As these structures occur in all sizes in crystalline rock, they are difficult to predict and pose a challenge for a potential repository. A hydraulic parameterization allowing for a fast assessment of water inflow and radionuclide migration potential is therefore of importance.

The fault zones aligning ductile shear zones correspond with the model of Faulkner et al. (2010) that features a highly fractured fault core or center, enclosing a damage zone with progressively decreasing fracturing towards the surrounding rock. However, structures in the Rotondo Granite are more variable. The four investigated structures are comparable to class 2A or 2B fault zones (Fault zones are confined within the shear zone extent or extend beyond its margins) as defined by Lützenkirchen (2002). In contrast to these standard models, the boundaries to the surrounding

rock are controlled by single main faults frequently following the mechanical contact of segregated mineral bands (Fig. 5b). Fracture frequencies spike close to the main fault planes and decrease in both directions away from them. Fracture densities decay slightly in the volume between the main fault planes but decay steeply towards the protolith.

Typical granite density of around  $2.6\text{ g/cm}^3$  was measured, agreeing with measurements by David et al. (2020), while the connected porosity of 0.9 to 1.1%, measured in the laboratory at atmospheric conditions, is similarly low compared to other granites (Géraud et al. 1995; Wenning et al. 2018; Möri et al. 2021; Drake et al. 2006; Aaltonen et al. 2016). In-situ porosity is expected to be even lower due to stress relief induced microcracks (Möri et al. 2021).

The distribution of permeability follows a non-linear trend from the center of the fault zone towards the surrounding rock as seen by Achtziger-Zupančič et al. (2016) for other fault zones in crystalline rocks. Lower permeabilities in the core correlate with less intense fracturing and partial healing of fractures (Figs. 3 and 4). Main flow paths are abundant in open fractures pervading the fault zones and reaching up to  $9 \cdot 10^{-14}\text{ m}^2$ . The matrix of the Rontondo Granite shows permeabilities around  $10^{-18}\text{ m}^2$  with about one order of magnitude variance, both for the flow cell measurements and point-scale gas probe permeameter tests. In comparison to a global permeability compilation (Achtziger-Zupančič et al. 2017), the matrix permeability around 1000m below ground surface (mbgs) is about an order of magnitude higher than the lower 10%-quantile regression representing the global matrix permeability. This might be caused by micro-fracturing in the excavation damage zone by spalling or by the drill-and-blast excavation of the 45 year old tunnel. The highest permeabilities in open fractures are well within the range of permeabilities yielded at 1000 mbgs for the upper 10%-quantile regression of the global database.

The hydraulic anisotropy follows the direction of shear as fractures with gouges and mica infill tend to have similar permeabilities to the rock matrix (Fig. 5). Similarly, structural asymmetry likely imprints an asymmetric distribution of hydraulic properties. The results shown here further demonstrate lower permeabilities in the vicinity of highly permeable fractures. Hydraulic communication across the fault zone substantially depends on the connectivity of fractures both in the fault center and the damage zone. The model is transitionally between the immature brittle and mature brittle fault zone as described by Wenning et al. (2018) for the Grimsel Granodiorite but shows a greater complexity. A repetitive pattern of fractured competent bands, sealed fracture surfaces, healed fractures and gouge or mica-filled fractures may indicate a self-similar flow pattern over scales comparable to the model shown by

Seebeck et al. (2014) for metamorphic greywacke and sandstone in the Taupo Rift (New Zealand).

## Conclusions

Understanding preferential flow paths in the context of a nuclear waste repository is paramount for site location and safety analysis, particularly with respect to water ingress and radionuclide transport. In crystalline rock, ductile shear zones imprinting mechanical weakness contrasts which are prone to brittle reactivation, are frequent. The development of a ductile shear zone in a brittle fault zone provides secondary, connected porosity for preferential flow paths.

Four such structures cropping out in the Bedretto Tunnel were analyzed in detail by scanline analysis in the tunnel and along cores. Core samples drilled from fault zones were tested in the lab for density, porosity and permeability by a gas probe permeameter and a hydraulic flow cell. Three boreholes were additionally tested by hydraulic packer tests.

The result is a detailed compilation of permeability on variable test volumes targeting the interplay of structural architecture and hydraulic behavior of brittle overprinted ductile shear zones. These zones frequently consist of two or more main faults as seen from fracture frequencies measured along scanlines, incorporating a volume which is less fractured. The faults often align with quartz-feldspar bands also incorporating lenses of sound or brecciated wall rock. The hydrogeology is dominated by channeled preferential flow paths along the bounding faults. Total and connected porosities are about 1.9–2.8% and 0.9–1.1%, respectively. The density is about  $2.6\text{ g/cm}^3$  throughout the fault zones. Single flow paths along partially open fractures may yield point-scale permeabilities  $>10^{-14}\text{ m}^2$ . If remineralized or coated by phyllosilicates, the permeability may be as low as the matrix permeability. Frequently, the lowest permeabilities are found in close proximity to highly permeable flow paths as potentially stabilizing factors. All these impacts give the appearance of a highly anisotropic distribution of permeability aligning with the direction of the fault zones, which is only interrupted by open fractures cross-cutting the entire structure. These observations extend across scales, as small structures are repetitive in larger structures.

**Acknowledgements** The publication is loosely based on the MSc-theses of Osten (2022) and Braun (2023). The latter received funding from the Federal Company for the Disposal of Radioactive Waste (BGE/BGETech) through the PRECODE project, who also provided the boreholes and cores in Sect. 3. We thank Joshua Braun and both funding organizations. Dr. Jacek Scibek is acknowledged for the provision of his gas probe permeameter and respective information. We also thank Alba Zappone for many discussions concerning structural geology and the entire BedrettoLab Team for providing access to the Bedretto Tunnel and OpTV logs. PAZ and TS are partially funded

through the PoroPermFlow project under the Excellence Strategy of the Federal Government and the German States. We also thank two anonymous reviewers for their comments and suggestions, which significantly improved the publication.

**Funding** Open Access funding enabled and organized by Projekt DEAL.

**Sample availability** Samples from boreholes BRI\_A\_01-03 are stored at the core repository of the Federal Company for the Disposal of Radioactive Waste (BGE/BGETech). Samples taken in Sects. 1 and 2 are available at the Department of Engineering Geology for a limited time.

**Conflict of interest** J. Osten, T. Schaber, G. Gaus, P. Hamdi, F. Amann and P. Achtziger-Zupančič declare that they have no competing interests.

**Open Access** This article is licensed under a Creative Commons Attribution 4.0 International License, which permits use, sharing, adaptation, distribution and reproduction in any medium or format, as long as you give appropriate credit to the original author(s) and the source, provide a link to the Creative Commons licence, and indicate if changes were made. The images or other third party material in this article are included in the article's Creative Commons licence, unless indicated otherwise in a credit line to the material. If material is not included in the article's Creative Commons licence and your intended use is not permitted by statutory regulation or exceeds the permitted use, you will need to obtain permission directly from the copyright holder. To view a copy of this licence, visit <http://creativecommons.org/licenses/by/4.0/>.

## References

- Aaltonen, I., Engström, J., Front, K., Gehor, S., Kosunen, P., Kärki, A., Mattila, J., Paananen, M., Paulamäki, S.: *Geology of Olkiluoto* (2016)
- Achtziger-Zupančič, P., Loew, S., Hiller, A., Mariétoz, G.: 3D fluid flow in fault zones of crystalline basement rocks (Poehla-Tellerhaeuser Ore Field, Ore Mountains, Germany). *Geofluids* **16**, 688–710 (2016)
- Achtziger-Zupančič, P., Loew, S., Mariétoz, G.: A new global database to improve predictions of permeability distribution in crystalline rocks at site scale. *J. Geophys. Res. Solid Earth* **122**, 3513–3539 (2017)
- Amberg, R.: *Der Furka-Basistunnel: Projekt und Bauausführung*. Schweizer Ing. Architekt **100**, 503–511 (1982)
- Bense, V., Gleeson, T., Loveless, S., Bour, O., Scibek, J.: Fault zone hydrogeology. *Earth Sci Rev.* **127**, 171–192 (2013)
- Berger, A., Mercolli, I., Herwegh, M., Gnos, E.: Geological map of the Aar Massif, Travetsch and Gotthard nappes—explanatory notes (2017)
- BGE, Bundesgesellschaft für Endlagersuche: *Zwischenbericht Teilgebiete gemäß § 13 StandAG, Zwischenbericht* (2020)
- Brace, W.F., Walsh, J.B., Frangos, W.T.: Permeability of granite under high pressure. *J. Geophys. Res.* **73**, 2225–2236 (1968)
- Braun, J.: PRECODE project: Hydro-mechanical characterization of the candidate location for grout injections at Bedretto Laboratory, Switzerland. RWTH Aachen University, Aachen (2023). Master's thesis
- Bredehoeft, J.D., Papadopoulos, S.S.: A method for determining the hydraulic properties of tight formations. *Water Resour. Res.* **16**, 233–238 (1980)
- Brixel, B., Klepikova, M., Jalali, M.R., Lei, Q., Roques, C., Kriestch, H., Loew, S.: Tracking fluid flow in shallow crustal fault zones: 1. Insights from single-hole permeability estimates. *J. Geophys. Res. Solid Earth* **125**, (2020)
- Caine, J.S., Evans, J.P., Forster, C.B.: Fault zone architecture and permeability structure. *Geology* **24**, 1025 (1996)
- Choi, J.-H., Edwards, P., Ko, K., Kim, Y.-S.: Definition and classification of fault damage zones: a review and a new methodological approach. *Earth Sci Rev.* **152**, 70–87 (2016)
- Clauser, C.: Permeability of crystalline rocks. *Eos Trans. Am. Geophys. Union* **73**, 233–238 (1992)
- Cooper Jr., H.H., Jacob, C.E.: A generalized graphical method for evaluating formation constants and summarizing well-field history. *Eos Trans. Am. Geophys. Union* **27**, 526–534 (1946)
- Cooper Jr., H.H., Bredehoeft, J.D., Papadopoulos, I.S.: Response of a finite-diameter well to an instantaneous charge of water. *Water Resour. Res.* **3**, 263–269 (1967)
- David, C., Nejati, M., Geremia, D.: On petrophysical and geomechanical properties of Bedretto Granite. Tech. rep. ETH, Zurich (2020)
- Drake, H., Sandström, B., Tullborg, E.-L.: *Svensk Kärnbränslehantering AB mineralogy and geochemistry of rocks and fracture fillings from Forsmark and Oskarshamn: compilation of data for SR-Can*. Tech. rep. Swedish Nuclear Fuel and Waste Management Co. (2006)
- Faulkner, D., Jackson, C., Lunn, R., Schlische, R., Shipton, Z., Wibberley, C., Withjack, M.: A review of recent developments concerning the structure, mechanics and fluid flow properties of fault zones. *J. Struct. Geol.* **32**, 1557–1575 (2010)
- Géraud, Y., Caron, J.-M., Faure, P.: Porosity network of a ductile shear zone. *J. Struct. Geol.* **17**, 1757–1769 (1995)
- Gischig, V.S., Giardini, D., Amann, F., Hertrich, M., Kriestch, H., Loew, S., Maurer, H., Villiger, L., Wiemer, S., Bethmann, F., Brixel, B., Doetsch, J., Doonechaly, N.G., Driesner, T., Dutler, N., Evans, K.F., Jalali, M., Jordan, D., Kittilä, A., Ma, X., Meier, P., Nejati, M., Obermann, A., Plenkers, K., Saar, M.O., Shakas, A., Valley, B.: Hydraulic stimulation and fluid circulation experiments in underground laboratories: Stepping up the scale towards engineered geothermal systems. *Geomech. Energy Environ.* **24**, (2020)
- Hardenbicker, L.R.: PRECODE project: rock-mechanical characterization of the candidate location for grout injections at Bedretto laboratory, Switzerland. RWTH Aachen University, Aachen (2023). unpublished Master Thesis
- Herwegh, M., Berger, A., Baumberger, R., Wehrens, P., Kissling, E.: Large-scale crustal-block-extrusion during late alpine collision. *Sci Rep* **7**, 413 (2017)
- Horner, D.R.: Pressure build-up in wells. In: *Proceedings third world petroleum congress*, pp. 503–521. (1951)
- Illman, W.A.: Strong field evidence of directional permeability scale effect in fractured rock. *J. Hydrol. Reg. Stud.* **319**, 227–236 (2006)
- ISRM: Suggested methods for the quantitative description of discontinuities in rock masses. *Int. J. Rock Mech. Min. Sci. Geomech. Abstr.* **15**, 319–368 (1978)
- ISRM: Suggested methods for determining water content, porosity, density, absorption and related properties and swelling and slakedurability index properties. *J. Rock Mech. Min. Sci. Geomech. Abstr.* **16**, 141–156 (1979)
- Jacob, C.E., Lohman, S.W.: Nonsteady flow to a well of constant drawdown in an extensive aquifer. *Eos Trans. Am. Geophys. Union* **33**, 559–569 (1952)
- Jordan, D.: Geological characterization of the Bedretto underground laboratory for geoenergies. ETH Zürich, Zürich (2019). Master's thesis
- Keller, F., Schneider, T.: *Geologie und Geotechnik*. Schweizer Ing. Architekt **100**, 512–520 (1982)
- Klinkenberg, L.J.: The permeability of porous media to liquids and gases. In: *Drilling and production practice*, pp. 200–2013. (1941)

- Kluge, C., Blöcher, G., Barnhoorn, A., Schmittbuhl, J., Bruhn, D.: Permeability evolution during shear zone initiation in low-porosity rocks. *Rock Mech Rock Eng* **54**, 5221–5244 (2021)
- Labhart, T.P.: 1251 val Bedretto: topographie : Landeskarte der Schweiz 1:25000 (1975)
- Lützenkirchen, V.H.: Structural geology and hydrogeology of brittle fault zones in the central and eastern Gotthard massif, Switzerland. ETH Zürich, Zürich (2002). Doctoral Thesis
- Lützenkirchen, V., Loew, S.: Late Alpine brittle faulting in the Rondo granite (Switzerland): deformation mechanisms and fault evolution. *Swiss J. Geosci.* **104**, 31–54 (2011)
- Ma, X., Hertrich, M., Amann, F., Bröker, K., Gholizadeh Doonechaly, N., Gischig, V., Hochreutener, R., Kästli, P., Krietsch, H., Marti, M., Nägeli, B., Nejati, M., Obermann, A., Plenkers, K., Rinaldi, A.P., Shakas, A., Villiger, L., Wenning, Q., Zappone, A., Bethmann, F., Castilla, R., Seberio, F., Meier, P., Driesner, T., Loew, S., Maurer, H., Saar, M.O., Wiemer, S., Giardini, D.: Multi-disciplinary characterizations of the BedrettoLab—a new underground geoscience research facility. *Solid Earth* **13**, 301–322 (2022)
- Marschall, P., Lunati, I.: GAM—gas migration experiments in a heterogeneous shear zone of the Grimsel test of the Grimsel test site (2006)
- Michibayashi, K., Togami, S., Takano, M., Kumazawa, M., Kageyama, T.: Application of scanning X-ray analytical microscope to the petrographic characterization of a ductile shear zone: an alternative method to image microstructures. *Tectonophysics* **310**, 55–67 (1999)
- Möri, A., Mazurek, M., Ota, K., Siitari-Kauppi, M., Eichinger, F., Leuenberger, M.: Quantifying the porosity of crystalline rocks by in situ and laboratory injection methods. *Minerals* **11**, (2021)
- Osten, J.: Hydro-mechanical characterization of candidate fault zones for FEAR in the Bedretto Tunnel, Switzerland. RWTH Aachen University, Aachen (2022). Master's thesis
- Rast, M., Galli, A., Ruh, J.B., Guillong, M., Madonna, C.: Geology along the Bedretto tunnel: kinematic and geochronological constraints on the evolution of the Gotthard Massif (Central Alps). *Swiss J. Geosci.* **115**, 8 (2022)
- Scibek, J.: Global compilation and analysis of fault zone permeability. McGill University, Montreal (2019). Doctoral Thesis
- Scibek, J., Annesley, I.R.: Permeability testing of drill core from basement rocks in the fault-hosted gryphon U deposit (eastern Athabasca basin, Canada): insights into fluid–rock interactions related to deposit formation and redistribution. *Nat. Resour. Res.* **30**, 2909–2956 (2021)
- Seebeck, H., Nicol, A., Walsh, J., Childs, C., Beetham, R., Pettinga, J.: Fluid flow in fault zones from an active rift. *J Struct Geol* **62**, 52–64 (2014)
- Sibson, R.H.: Fault rocks and fault mechanisms. *J. Geol. Soc.* **133**, 191–213 (1977)
- Sibson, R.H.: Continental fault structure and the shallow earthquake source. *J. Geol. Soc.* **140**, 741–767 (1983)
- Shea, W.T., Kronenberg, A.K.: Strength and anisotropy of foliated rocks with varied mica contents *Journal of Structural Geology* **15**(9–10), 1097–1121 (1993). [https://doi.org/10.1016/0191-8141\(93\)90158-7](https://doi.org/10.1016/0191-8141(93)90158-7)
- Snowdon, A.P., Normani, S.D., Sykes, J.F.: Analysis of crystalline rock permeability versus depth in a Canadian precambrian rock setting. *J. Geophys. Res. Solid Earth* **126**, (2021)
- Stenvall, C.A., Fagereng, Å., Diener, J.F.A.: Weaker Than Weakest: On the Strength of Shear Zones Abstract Plain Language Summary Key Points *Geophysical Research Letters* **46**(13), 7404–7413 (2019). <https://doi.org/10.1029/2019GL083388>
- Tanikawa, W., Shimamoto, T.: Comparison of Klinkenberg-corrected gas permeability and water permeability in sedimentary rocks. *Int. J. Rock Mech. Min. Sci.* **46**, 229–238 (2009)
- Theis, C.V.: The relation between the lowering of the Piezometric surface and the rate and duration of discharge of a well using groundwater storage. *Trans. Am. Geophys. Union* **16**, 519 (1935)
- Torabi, A., Ellingsen, T.S.S., Johannessen, M.U., Alaei, B., Rotevatn, A., Chiarella, D.: Fault zone architecture and its scaling laws: where does the damage zone start and stop? *Special Publications 496*. Geological Society, London, pp. 99–124 (2020)
- Tourigny, G., Tremblay, A.: Origin and incremental evolution of brittle/ductile shear zones in granitic rocks: natural examples from the southern Abitibi Belt, Canada. *J Struct Geol* **19**, 15–27 (1997)
- Tsang, C.-F., Neretnieks, I., Tsang, Y.: Hydrologic issues associated with nuclear waste repositories. *Water Resour. Res.* **51**, 6923–6972 (2015)
- Vauchez, A.: The development of discrete shear-zones in a granite: stress, strain and changes in deformation mechanisms. *Tectonophysics* **133**, 137–156 (1987)
- Volpe, G., Pozzi, G., Colletini, C., Spagnuolo, E., Achtziger-Zupančič, P., Zappone, A., Aldega, L., Meier, M., Giardini, D., Cocco, M.: Laboratory simulation of fault reactivation by fluid injection and implications for induced seismicity at the BedrettoLab, Swiss Alps. *Tectonophysics* **862**, (2023)
- Wehrens, P., Baumberger, R., Berger, A., Herwegh, M.: How is strain localized in a meta-granitoid, mid-crustal basement section? Spatial distribution of deformation in the central Aar massif (Switzerland). *J Struct Geol* **94**, 47–67 (2017)
- Wenning, Q.C., Madonna, C., de Haller, A., Burg, J.-P.: Permeability and seismic velocity anisotropy across a ductile–brittle fault zone in crystalline rock. *Solid Earth* **9**, (2018)
- Witherspoon, P.A., Bodvarsson, G.S.: Geological challenges in radioactive waste isolation—fourth worldwide review. Tech. Rep. LBNL-59808. Ernest Orlando Lawrence Berkeley National Laboratory, University of California (2006)

**Publisher's Note** Springer Nature remains neutral with regard to jurisdictional claims in published maps and institutional affiliations.